The Crescent Nebula and its hundreds of line-of sight stars as seen with the imaging FTS SITELLE

Marianne Ruest[a,c], Camille Poitras[a,c], Laurent Drissen[a,c], and Nicole St-Louis[b,c]

[a]Département de physique, de génie physique et d'optique, Université Laval, Québec, Canada
[b]Département de Physique, Université de Montréal, Campus MIL, Montréal, Canada
[c]Centre de Recherche en Astrophysique du Québec

ABSTRACT

The Crescent Nebula, NGC 6888, has long been the muse of many scientific and amateur research. However, the recent data provided by SITELLE, a wide-field imaging Fourier transform spectrometer at the Canada-France-Hawaii telescope call for new analysis and conclusions. The spectral cubes offer a field of view of 11×11 arcminutes^2 and have been acquired trough 5 different filter-selected bands covering the optical waveband (from 350 to 680 nm), allowing 23 characteristic emission optical lines to be described with a spectral resolution reaching up to 2500. Doppler shifting allow two-components velocity fits, describing the multi-layered bubble's kinematics. The sulfur doublet describes electronic densities. Other faint lines (including [NII] 5755, [OIII] 4363 and NeIII 3868) are essential to determine accurate temperatures and abundances. Emission lines are key to this nebular research, but absorption lines in the spectrum of hundreds of field stars are also studied. All this leads to a more complete physical description of NGC 6888, its central star WR136 and the stars present in the field of view.

Keywords: techniques: Fourier transform spectroscopy - ISM: bubbles - stars: Wolf-Rayet

1. INTRODUCTION

The study of nebulae around Wolf-Rayet (WR) stars can hint us about the mass-loss history of massive stars and about the enrichment of the interstellar medium (ISM). We have observed the southwestern part of the wind-blown bubble NGC 6888, a WR nebula, using the Canada–France–Hawaii Telescope's imaging Fourier transform spectrometer SITELLE.[1] This instrument and the unique characteristics of the data it provides are put forward in this paper.

1.1 NGC 6888

A Wolf-Rayet nebula is formed when the strong wind from a massive star ejects material that eventually interacts with the surrounding interstellar medium, starting during the main sequence and then the following evolutionary phases: red supergiant or Luminous Blue Variable, and then Wolf-Rayet. Although NGC 6888 was first classified as a supernova remnant (SNR),[2] its status as a Wolf-Rayet bubble nebula came soon after. The star responsible for its formation and ionization, WR 136 (HD 192163), is of subtype WN6: its spectrum is dominated by broad emission lines of helium and nitrogen[3] and its effective temperature approaches 70 000K.[4]

The helium and nitrogen enrichment, as well as the oxygen deficiency observable for this type of star's surrounding are explained by a transport of material from the core (where the CNO cycle dominated the energy production during the main sequence) to the shell during the red supergiant (RSG) phase of the star.[5]

NGC6888's morphology, as described recently,[6,7] has two main shells: the outer shell, round, homogeneous and dominated by the [OIII] 5007 emission line, and the inner shell, ellipsoidal, filamentous and abundant in nitrogen have been created respectively during the stellar transition from the main sequence to the RGB phase, and from the RGB to the WR phase, also called the *three-wind-model*.[8] Once a massive star has reached the WR phase, its fast wind will sweep up the material ejected during the immediate precursor (in this case, RSG)

E-mail: marianne.ruest.2@ulaval.ca
Paper: 12184-237

slow wind,[9] creating dynamical features as seen in Figure 1. Some also add[10] that the former is a mix of gas and dust whereas the latter is mostly gas, confirming the hypothesis that it has been projected by a previous star phase into the ISM (shocks).

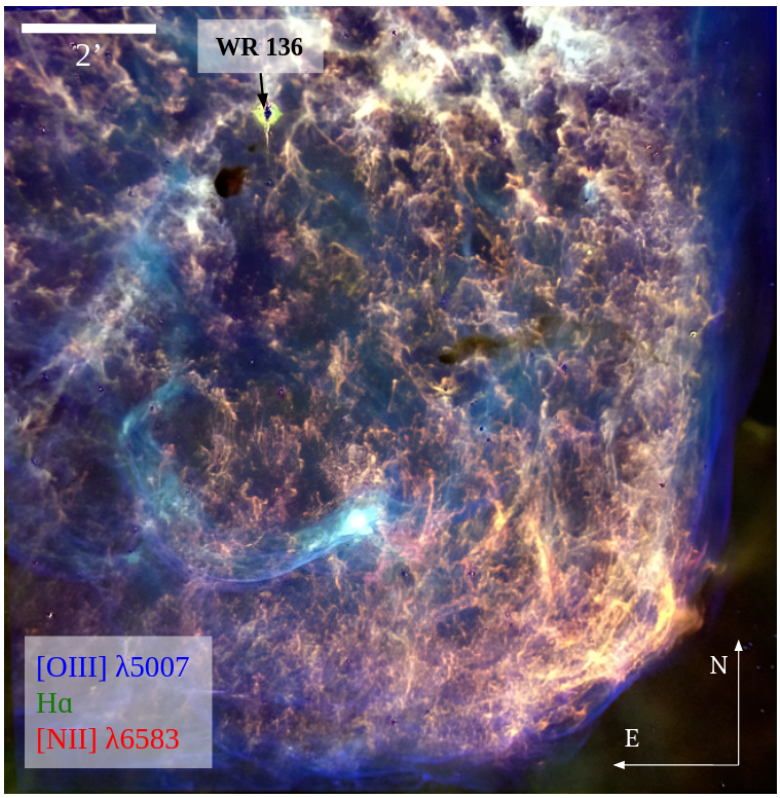

Figure 1: SITELLE's field of view showing the southwestern part of NGC 6888 with colored lines: [OIII] λ5007 in blue, Hα in green and [NII] λ6583 in red.

Another unsolved mystery is that NGC 6888's second layer is clearly composed of two bipolar lobes, which hints to the existence of asymmetric pre-Wolf-Rayet winds and/or a velocity gradient between the star and the ISM.[11] Work is still in progress to assess the extent of this phenomenon.

1.2 Motivations

This work was undertaken to improve the spectroscopic data available for the southwestern part of NGC 6888 where optical lines are present. A field of view of 11×11 arcminutes is by far the largest spatially resolved hyperspectral sampling ever acquired of the Crescent Nebula. The goal of this work is to wrap up information from this rich dataset to describe things like features and morphology, kinematics, electronic densities and abundance distribution to collect all the necessary information to create its most complete evolutionary model using, for instance, PyCloudy.[12]

In addition, an ongoing spectral classification of the hundreds of stars along the line of sight tests the rather promising capabilities of SITELLE in its measurement of absorption lines.

At the time of writing this paper, a second field is being processed in its northern part which will allow an even more complete spatial and kinematic description of NGC 6888.

1.3 SITELLE

SITELLE is an imaging Fourier transform spectrometer in the optical (350 to 850 nm), based at the Canada-France-Hawaï Telescope (CFHT). Its raw data are called interferograms and Fourier transforms are used to convert them into actual spectral data cubes of 2048×2064 spaxels, covering a field of view (FOV) of 11×11 arcminutes. The spatial sampling is thus of $0.32''$, which allows to properly sample the point spread function. SITELLE's spectral resolution can reach up to 10 000, but it varied between 575 and 2500 for our data. More information on SITELLE is presented by Drissen et al. in these proceeding.

2. DATA AND ANALYSIS

2.1 The dataset

Table 1 presents the properties of the data cubes, obtained in 2017 and 2018, while Figure 2 illustrates the entire dataset with fits to an integrated region of the nebula. The data almost cover the entire visible band, with different spectral resolutions, providing a unique dataset of diagnostic lines for the analysis of the ionization properties, chemical abundances and kinematics of the nebula. Point laces between lines in the fitted model, amplified by the logarithmic scale of the graph, are not noise. They are the sidelobes of the sinc function, typical of Fourier transform spectrometers.

Table 1: Observational parameters at data acquisition.

Characteristics	SN3	SN2	SN1	C2	C1
Spectral range [Å]	6470-6850	4820-5130	3630-3860	5590-6250	3850-4900
Number of steps	421	225	103	466	405
Total acquisition time [h]	2.15	1.88	1.44	3.62	3.37
Spectral resolution R	2500	1000	575	1700	650
Seeing at acquisition (arcsec)	1.4	1.0	0.8	1.0	1.0

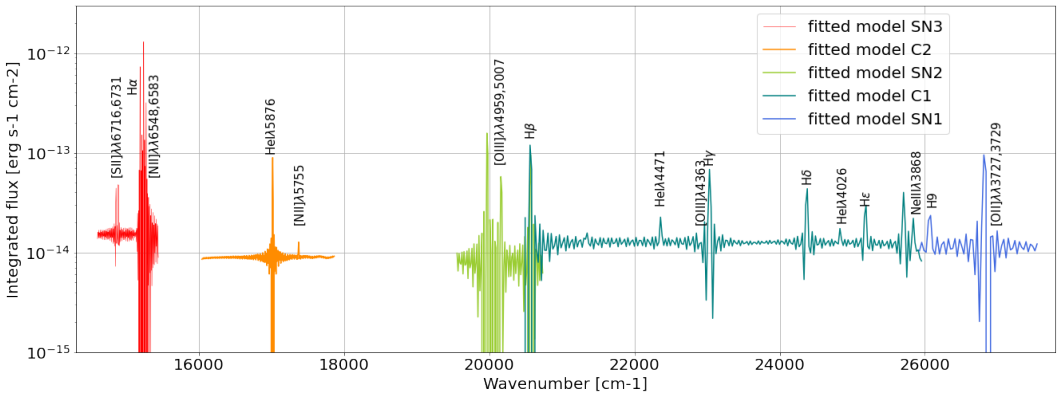

Figure 2: Total fitted spectrum including all 5 data cubes. The varying continuum level reflects the Moon phase during which the data were obtained. It is properly adjusted ans subtracted to measure the line fluxes.

The SN3 filter is the most popular SITELLE filter since it includes the bright Hα line along with other important diagnostic lines such as the sulfur doublet [SII]$\lambda\lambda$6717,6731 for electronic densities and the nitrogen doublet [NII]$\lambda\lambda$6548,6583 for abundance comparison and temperature determination. The SN2 filter is used for the Hβ line that, once compared with the Hα line, provides a map of the extinction along the line of sight. The forbidden oxygen doublet [OIII]$\lambda\lambda$4959,5007 is used for abundance comparison and temperature determination.

The C2 filter was designed to study the faint auroral [NII]λ5755 line which, compared with the nitrogen doublet from the SN3 filter leads to a direct measurement of the electronic temperature, and hence a precise chemical abundances. C2 also includes the HeIλ5876 line to measure the helium abundance.

C1 is the widest filter; it provides information on the Balmer decrement from Hβ to Hε, therefore extending the wavelength range available for a precise determination of the extinction. It also includes the weak HeIλ4471 and HeIλ4026 lines (for helium abundance) as well as the auroral line [OIII]λ4363, which when compared with the oxygen doublet from the SN2 filter, is used for the electronic temperature determination in a different ionization zone than the [OIII] lines. The NeIIIλ3868 line will also provide an important diagnostic of the star's evolutionary path.

Finally, the SN1 filter was chosen to map the forbidden oxygen doublet [OII]$\lambda\lambda$3727,3729, (unresolved at our spectral resolution) which will allow to describe the ionisation flux as a function of the distance from the star.

2.2 Data analysis with ORCS

Data reduction and analysis require specialized software that provide both precision and adaptability, which is exactly what ORB and ORCS[1,13,14] do.

An example of a fit over an integrated region of the nebula with a diameter of 20 pixels is shown in Figure 3 and represents the C1 filter spectrum and its 11 emission lines (H8 and HeIλ3888 are superimposed so they are fitted only once). A sincgauss function (the instrumental line shape - a sinc - convoluted with a gaussian to take into account turbulence and expansion of the nebula) is used. ORCS provide line width, centroid and height with their uncertainties for each line.

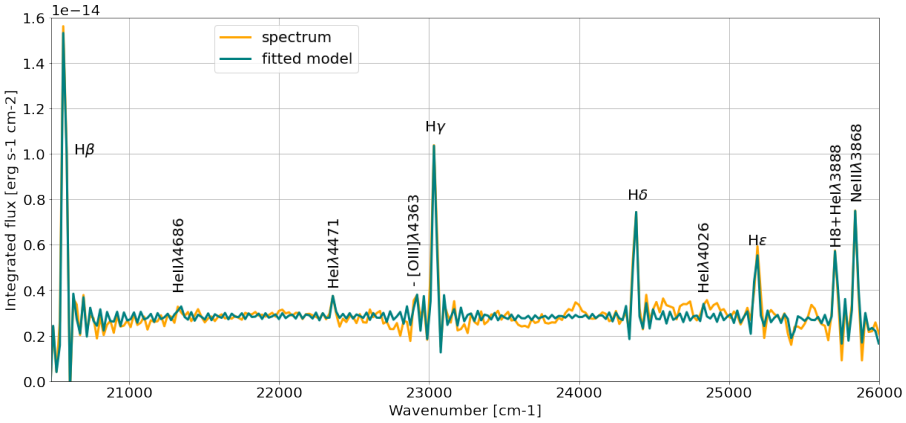

Figure 3: Spectrum and fitted model for the C1 datacube of NGC 6888.

The Balmer decrement is pretty obvious in this spectrum, in addition to helium lines, as expected for a WR nebula around a WN6 star. We can also see the faint auroral [OIII]λ4363 line a strong neon line (NeIIIλ3868). The sidelobes of the sinc function are properly fitted. On the other hand, the background continuum is not adjusted properly in this example, hence the mismatch between the observed spectrum and its fit outside the emission lines.

In addition to fitting the integrated spectrum of selected regions, ORCS provides a map of each line flux by fitting the spectra of the 4 million individual pixels of the cubes. Figure 4 shows examples of four lines very rarely mapped on such an extended field of view.

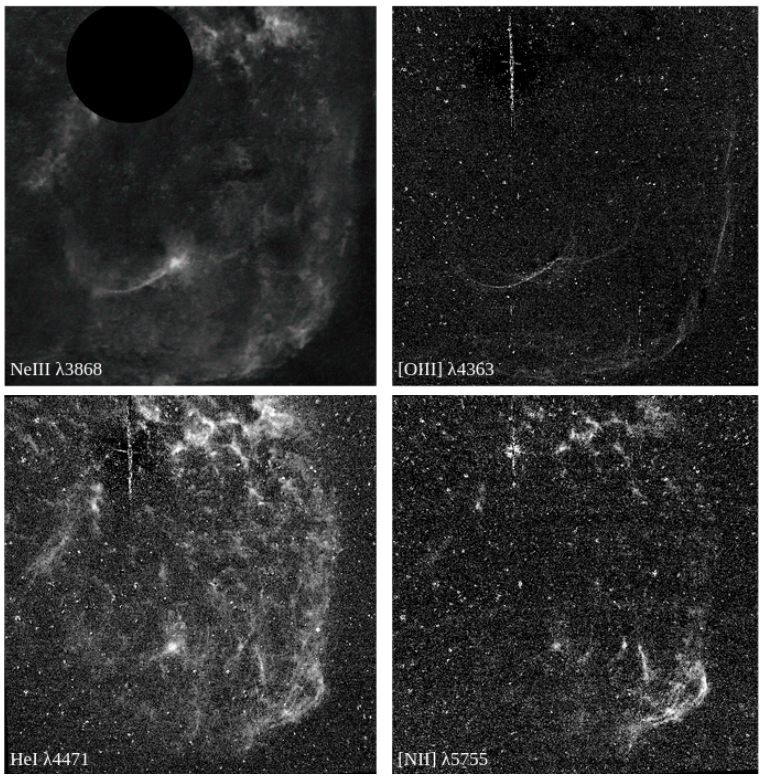

Figure 4: Faint and auroral lines

3. FILAMENTOUS STRUCTURES

As seen in image 1, turbulences and non-uniformities in the structure of the shells are observable. Those are Rayleigh-Taylor instabilities and are engendered whenever a hot and dense fluid collisions with a colder more tenuous one.[15] This shows that the first smooth layer, emitted during the red supergiant phase is now being crashed into by the denser second layer, characteristic of a fast WR wind.[16] It is also possible to assess that the first layer collided rather smoothly with the ISM.

The blowout visible in the lower right part of the nebula might be caused by a rupture in the hot dense shell structure[17] possibly due to Vishniac instabilities. Clumpy and filamentary density structures are thus likely created by both the Vishniac and Rayleigh-Taylor instabilities.

4. ELECTRONIC DENSITIES AND TEMPERATURES

Electronic densities and temperature vary with one another in nebulae. Here we assume an electron temperature of $T_e = 10\,000\,\mathrm{K}$ as a safe bet for first approximation, but a detailed analysis taking into account the measurements of the auroral lines discussed above will be undertaken later using a Monte Carlo approach to simultaneously determine both density and temperature.

Electronic densities are determined using the ratio of the forbidden sulfur lines [SII]λ6717 and [SII]λ6731. The theoretical relation between line ratio and electronic densities that has been used for decades has been updated[18] to a systematically 20-22% lower value due to new atomic data. This new electronic density function is shown in equation 1:

$$\log\big(n_e[\mathrm{cm}^{-3}]\big) = 0.0543\tan(-3.0553R + 2.8506) + 6.98 - 10.6905R + 9.9186R^2 - 3.5442R^3, \qquad (1)$$

where R is the flux ratio $R = \frac{I_{6716}}{I_{6731}}$, and n_e is the electronic density.

The star being so hot, the [SII] lines are very weak, so it is impossible to map the electronic density pixel by pixel. We instead select integrated regions to maximise the signal-to-noise ratio over the most luminous regions. Those are shown in figure 5 and their color represents electronic densities, which vary from 0 to 200 cm^{-3}, values that are quite low but not uncommon for WR nebulae.

The next step of this research category will be to determine electron temperatures from different independent ratios, starting with the oxygen lines. The equation that will be used is shown in eq 3.[18]

$$R = \frac{I_{4959} + I_{5007}}{I_{4363}} \tag{2}$$

$$T_e = 5294(\log(R) - 0.848)^{-1} + 19047 - 7769\log(R) + 944\log(R)^2 \tag{3}$$

Similar equations are used for the nitrogen line fluxes. Chemical abundances will then be determined.

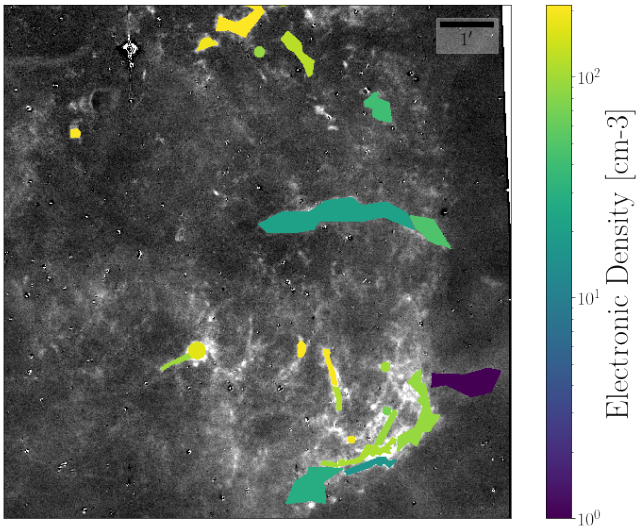

Figure 5: Electronic densities for selected regions. The background monochrome image is the map of the [SII] doublet.

5. KINEMATICS

NGC 6888 is an expanding gas and dust bubble[19] driven by the dense, fast WR wind from the central star. That motion is observable with SITELLE data.

The spectral cube SN3 has the best spectral resolution, which is crucial when determining radial velocities via Doppler shifting. It is however important to keep in mind that a wind-blown bubble expands, so that a one velocity fit is not representative of all the layers visible in one line of sight. So spectral resolution is key mostly when comes the time to distinguish *at least* two velocity components.

Figure 6 is a qualitative Doppler map, obtained by combining in different colors consecutive channels that make up the Hα line. The expansion of the bubble is evident.

In order to obtain a more quantitative measurement of the bubble expansion, we have used ORCS to fit a double component velocity model using two sinc functions. An example of two component velocity fit is shown in figure 7, where the observed Hα line in green, while the single component sincgauss model is illustrated in yellow. The red and blue fits are respectively the redshifted and blueshifted velocity components. This figure shows that it is possible to obtain a fit as good as the single component with two sinc functions for a region as small as 9 $\times$ 9 spaxels.

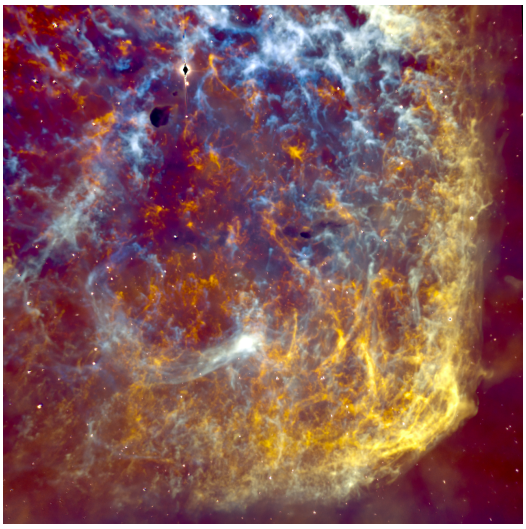

Figure 6: Quantitative radial velocity map. Red represents gas drifting away while blue gas is approaching us.

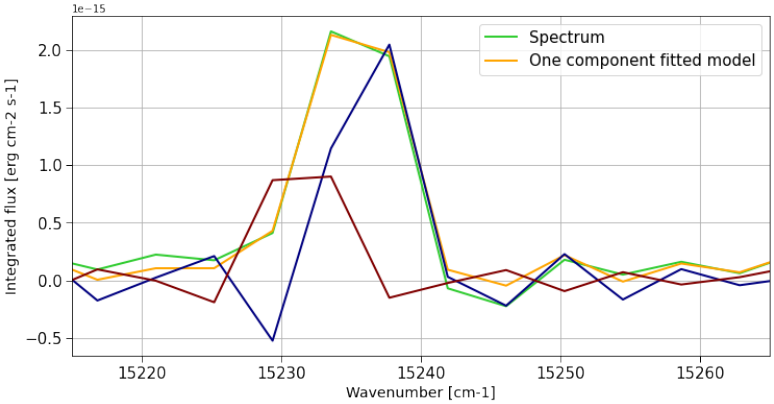

Figure 7: Spectrum with two velocity fits for the Hα line. The blue line represents the whereas the dark red line represents the receding gas for a small group of spaxels.

Complete double velocity maps have been produced and calibrated and are represented as a histogram in Figure 8. The expansion velocity we can draw from this histogram is around 45 km s^{-1} up to 100 km s^{-1}, in perfect agreement with previous work based on long-slit spectra.[6,7,20]

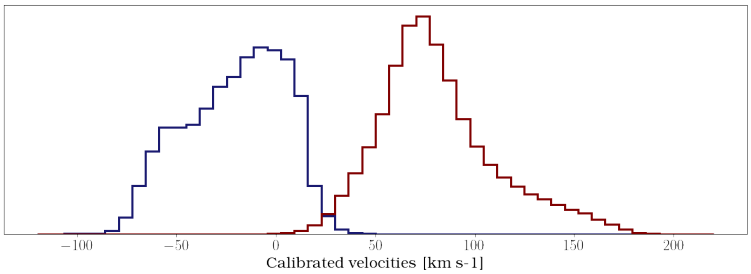

Figure 8: Velocity dispersion histogram

6. STELLAR SPECTRA

The last "E" in SITELLE stands for Emission. This instrument was indeed designed to study extended emission line sources such as nebulae and star-forming galaxies, because Fourier transform spectrometers are notoriously less efficient than dispersive instruments for continuum and absorption line study of faint sources. This is because with an FTS the spectrum of the source is acquired by obtaining a series of images covering the entire bandpass defined by the filter, at different optical path differences of the interferometer, thus building an interferogram which is then Fourier transformed.[21] Hence, the photon noise from the entire bandpass affects each spectral element of the spectrum thus obtained. Nevertheless, absorption spectroscopy of astronomical sources is feasible with an FTS, as demonstrated by many, almost exclusively on bright stars in the near-infrared regime.[22–24]

The data cube of NGC 6888 obtained with the C1 filter is particularly well suited to demonstrate the feasibility and limits of SITELLE for absorption work as it covers a spectral bandpass (389 - 484 nm) often used to classify stellar spectra .

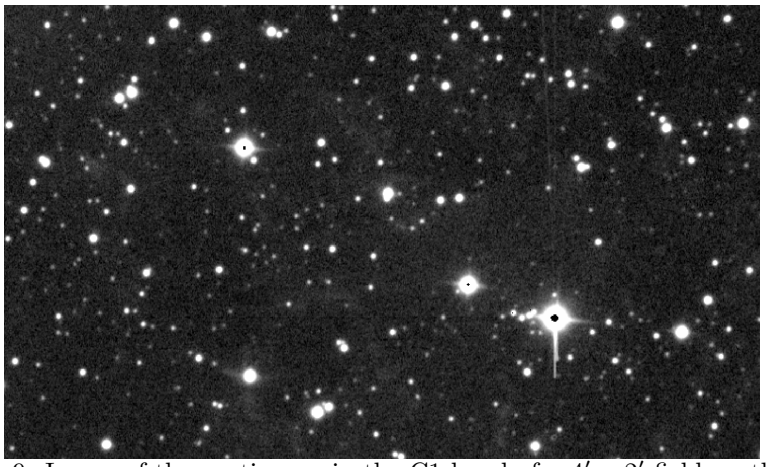

Figure 9: Image of the continuum in the C1 band of a $4' \times 2'$ field south-west of WR136, representing 8% of the total field of view.

6.1 Spectra extraction process

The need to study the characteristics of not a dozen but several hundred stars (see Figure 9) in the SITELLE data cubes inevitably led to the development of a routine. The task of this novel routine allows two main applications:

Stars detection - Consists of automatically detecting the position of the stars. The approach is based on the "DAOStarFinder" class which allows to targets objects with an intensity greater than a minimum selected threshold and to obtain some parameters such as the instrumental magnitude.[25]

Spectra extraction - Spectrum extraction and background removal are two tools already implemented in ORCS. The addition of an automation process thus completes the pre-existing functions of this data analysis software by obtaining the spectra effectively without active participation.

Automatic star detection in the C1 data cube of NGC 6888 targeted over a thousand stars with a full width at half-maximum (FWHM) larger than 3 pixels and minimum intensity threshold of $13^{*}\sigma$ above the background. Following the automatic extraction of their spectra, we have observed that some of them were partly or even totally not suitable for further analysis. Of these faulty spectra, most were contaminated by the signal's spectrum of the nebula or the Wolf-Rayet star, and few were the result of problems that can arise with the DAOStarFinder algorithm. Indeed, the techniques of detection used can be misleading in cases where the intensity of the background fluctuates or unwanted noise is recorded (e.g. cosmic-rays), because the algorithm do not differentiate between these variations and those specific to stars. Hence, possible changes to this method

implemented in the new routine may be made if speed and immediate precision become considerable criteria. Nevertheless, for the NGC 6888 data cube, the method still remained sufficient and the defective spectra were simply removed manually. Ultimately, out of the hundreds of candidates detected, we have selected just over four hundred stars to move on to the next step: the spectral classification.

6.2 Results

6.2.1 Spectral classification

The models of stellar spectra available in the atlas by R. O. Gray[26] are used for the current distribution of stars into categories. So far, the spectral classification shows three more common types, namely A, F and G. A few rarer stars can also be classified as K- and M-types or in categories belonging to other classification systems such as carbon stars.

Figure 10 shows the spectra of type A, G, and K stars and a carbon star. In this sample, we can easily discern the most important absorption lines that dominate each of the spectral classes, including the hydrogen lines (Hβ, Hγ, Hδ, Hϵ, H8), the molecular band of CH, also called "G-band", the CaII H & K doublet at 3933-68 and the TiO bands. As for the carbon star, it is possible to distinguish the imposing bands of carbon molecules such as those of C_2, CN and CH. Weaker lines can also be recognized in several extracted spectra as for example the Ca I and Mn I lines of the spectrum of the G-type star presented (see Fig 10). Therefore, the distinction of these features that can be identified and quantified clearly demonstrates the possibilities that the C1 filter has to offer for the study of stellar absorption spectra in addition to leading to an interesting and diverse classification.

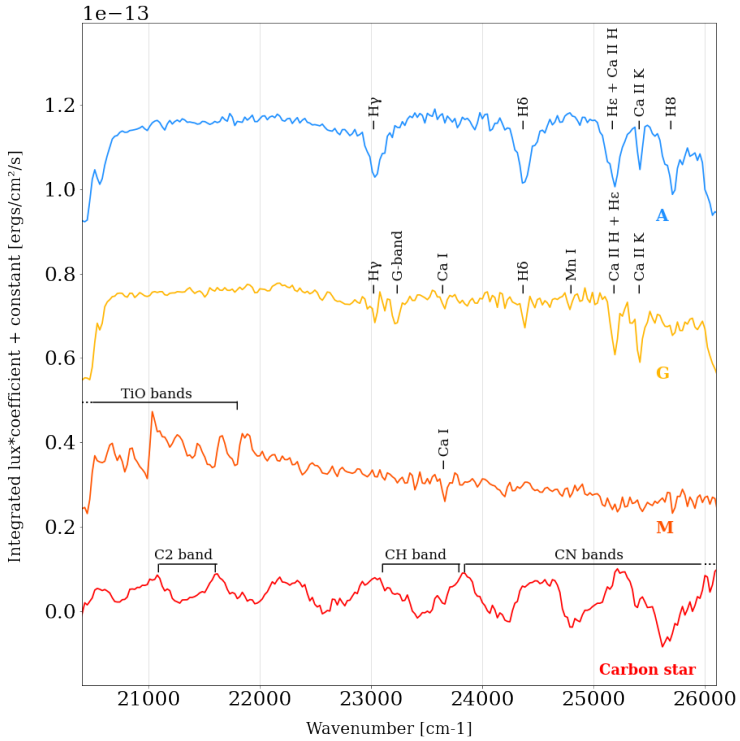

Figure 10: Examples of stellar spectra extracted with ORCS in the data cube of NGC 6888 with the C1 SITELLE filter. From to to bottom, we can observe A-, G- and M-type stars, and also a carbon star. The main features of each spectrum are labeled. The normalized flux is multiplied by a coefficient to have spectra of the same size and added to a constant to have a vertical separation.

The central ionizing star of the Crescent nebula, WR 136, is of course present in the field. Its particular spectrum rich in helium and nitrogen, as well as weak hydrogen components (see Figure 11) classifies it in the

WN6(h)-s spectral subtype.[27] This spectrum was extracted from a region of the point spread function away from the central, saturated region.

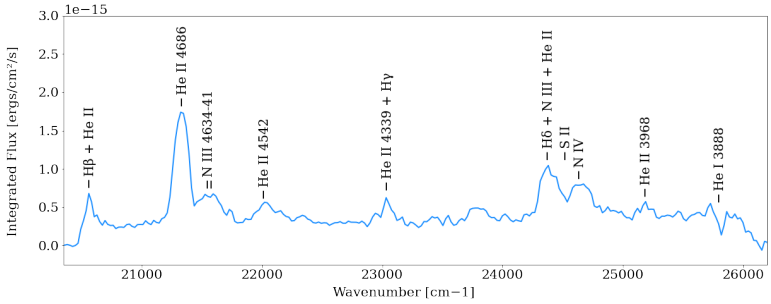

Figure 11: The C1 spectrum of WR 136 extracted from a region of the PSF to avoid the saturated zone. The strong emission lines and the He I λ 3888 absorption line are labeled.

6.2.2 Spectrum slope and interstellar CaII lines

The stellar dataset in the line of sight to NGC 6888 also allows to observe two interesting parameters:

(i) Slope. The variable inclination slope of the A-type stars could be an indicator of interstellar extinction. A decreasing curve would characterize a more or less significant absorption and reddening of the star while an increasing one indicate a very low absorption. Figure 12 shows examples these two distinct situations. Here we measured the slope of the spectra by a linear regression estimated by the method of least squares with a dataset between 20400 - 25600 cm^{-1} to exclude filter edges.

(ii) Interstellar Ca II lines. Previous work has shown that the intensities of the narrow interstellar CaII H & K doublet (3933 - 3968 Å) lines may be a distance-determining parameter for early-type stars.[28] In our spectra of hotter stars, these well-known interstellar CaII lines can be recognized, but the resolution limits the observation of the H-line which intertwines with the imposing Hϵ feature. Nevertheless, the different strengths of the K-lines remain interesting to study the relation between its intensity and the distance from objects.

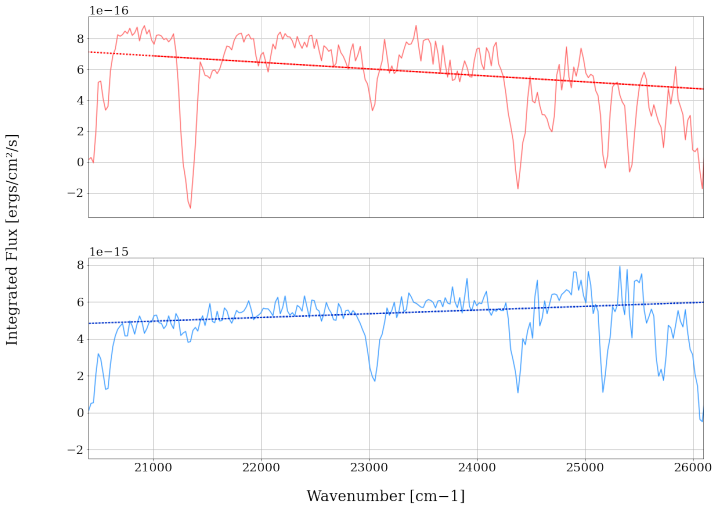

Figure 12: Representations of spectra slopes with linear regression.

7. CONCLUSIONS

Using five SITELLE filters, the data of the southwestern part of the crescent nebula NGC 6888 allows us to describe spatial distributions numerous emission lines as well as detail the filamentous structures present in this expanding bubble and the dynamical processes creating them. The electronic densities have been determined to be less than 200 e^- cm^{-3}, and temperatures are on their way to be calculated using the auroral lines [NII]λ5755 and [OIII]λ4363. Doppler shift and double velocity fitting allow us to target velocity of the expanding bubbles around 50 - 100 km s^{-1}. We also demonstrate that SITELLE, although not designed for the study of absorption lines because of its intrinsic FTS design, could nevertheless be used to study stellar field such as open and globular clusters.

ACKNOWLEDGMENTS

This paper is based on data obtained with the Canada-France-Hawaii Telescope (CFHT), which is operated by the National Research Council of Canada, the Institut National des Sciences de l'Univers of the Centre National de la Recherche Scientifique of France and the University of Hawaii.The authors wish to recognize and acknowledge the very significant cultural role that the summit of Mauna Kea has always had within the indigenous Hawaiian community. We are most grateful to have the opportunity to conduct observations from this mountain. The observations were obtained with SITELLE, a joint project of Université Laval, ABB, Université de Montréal and the CFHT, with support from the Canada Foundation for Innovation, the National Sciences and Engineering Research Council of Canada (NSERC) and the Fonds de Recherche du Québec - Nature et Technologies (FRQNT). LD and NStL are grateful to NSERC and FRQNT for financial support.

REFERENCES

[1] Drissen, L., Martin, T., Rousseau-Nepton, L., Robert, C., Martin, R. P., Baril, M., Prunet, S., Joncas, G., Thibault, S., Brousseau, D., Mandar, J., Grandmont, F., Yee, H., and Simard, L., "SITELLE: an Imaging Fourier Transform Spectrometer for the Canada–France–Hawaii Telescope," *Monthly Notices of the Royal Astronomical Society* **485**, 3930–3946 (May 2019).

[2] Parker, R. A. R., "Physical Conditions in the Cygnus Loop and Some Other Possible Supernova Remnants.," *The Astrophysical Journal* **139**, 493 (Feb. 1964). ADS Bibcode: 1964ApJ...139..493P.

[3] B.W, C. and D.A, O., [*An introduction to modern astrophysics*], 2ed., pearson ed. (2007).

[4] Reyes-Pérez, J., Morisset, C., Peña, M., and Mesa-Delgado, A., "A consistent spectral model of WR 136 and its associated bubble NGC 6888," *Monthly Notices of the Royal Astronomical Society* **452**, 1764–1778 (Sept. 2015).

[5] Parker, R. A. R., "The [N II]/Halpha ratio in NGC 6888.," *The Astrophysical Journal* **224**, 873–884 (Sept. 1978). ADS Bibcode: 1978ApJ...224..873P.

[6] Treffers, R. R. and Chu, Y. H., "Galactic ring nebulae associated with Wolf-rayet stars. VII. The nebula G 2.4 +1.4.," *The Astrophysical Journal* **254**, 132–135 (Mar. 1982). ADS Bibcode: 1982ApJ...254..132T.

[7] Fernández-Martín, A., Martín-Gordón, D., Vílchez, J. M., Montero, E. P., Riera, A., and Sánchez, S. F., "Ionization structure and chemical abundances of the Wolf-Rayet nebula NGC 6888 with integral field spectroscopy," *Astronomy & Astrophysics* **541**, A119 (May 2012).

[8] Garcia-Segura, G., Langer, N., and Mac Low, M.-M., "The hydrodynamic evolution of circumstellar gas around massive stars. II. The impact of the time sequence O star -> RSG -> WR star.," *Astronomy and Astrophysics, v.316, p.133-146* **316**, 133 (Dec. 1996).

[9] Crowther, P. A., "Physical Properties of Wolf-Rayet Stars," *Annual Review of Astronomy & Astrophysics, vol. 45, Issue 1, pp.177-219* **45**, 177 (Sept. 2007).

[10] Rubio, G., Toalá, J. A., Jiménez-Hernández, P., Ramos-Larios, G., Guerrero, M. A., Gómez-González, V. M. A., Santamaría, E., and Quino-Mendoza, J. A., "Unveiling the stellar origin of the Wolf–Rayet nebula NGC 6888 through infrared observations," *Monthly Notices of the Royal Astronomical Society* **499**, 415–427 (Oct. 2020).

[11] Meyer, D. M. A., "On the bipolarity of Wolf-Rayet nebulae," *Monthly Notices of the Royal Astronomical Society* **507**, 4697–4714 (Nov. 2021). ADS Bibcode: 2021MNRAS.507.4697M.

[12] Morisset, C., "pyCloudy: Tools to manage astronomical Cloudy photoionization code," *Astrophysics Source Code Library* , ascl:1304.020 (Apr. 2013). ADS Bibcode: 2013ascl.soft04020M.

[13] Martin, T. and Drissen, L., "Calibrations of SITELLE's first data release," *arXiv:1706.03230 [astro-ph]* (June 2017). arXiv: 1706.03230.

[14] Martin, T., Drissen, L., and Prunet, S., "Data reduction and calibration accuracy of the imaging Fourier transform spectrometer SITELLE," *Monthly Notices of the Royal Astronomical Society* **505**, 5514–5529 (Aug. 2021). ADS Bibcode: 2021MNRAS.505.5514M.

[15] Toalá, J. A. and Arthur, S. J., "RADIATION-HYDRODYNAMIC MODELS OF THE EVOLVING CIRCUMSTELLAR MEDIUM AROUND MASSIVE STARS," *The Astrophysical Journal* **737**, 100 (Aug. 2011). Publisher: American Astronomical Society.

[16] Reyes-Iturbide, J., Velázquez, P. F., and Rosado, M., [*3D numerical model for NGC 6888 Nebula*] (Jan. 2015). Conference Name: Wolf-Rayet Stars Pages: 363 ADS Bibcode: 2015wrs..conf..363R.

[17] Pittard, J. M., "Self-sealing shells: blowouts and blisters on the surfaces of leaky wind-blown bubbles and supernova remnants," *Monthly Notices of the Royal Astronomical Society* **435**, 3600–3613 (Nov. 2013).

[18] Proxauf, B., Öttl, S., and Kimeswenger, S., "Upgrading electron temperature and electron density diagnostic diagrams of forbidden line emission," *Astronomy & Astrophysics, Volume 561, id.A10, <NUMPAGES>4</NUMPAGES> pp.* **561**, A10 (Jan. 2014).

[19] Chu, Y. H. and Treffers, R. R., "Galactic ring nebulae associated with Wolf-rayet stars. III. Region-type nebulae.," *The Astrophysical Journal* **250**, 615–620 (Nov. 1981). ADS Bibcode: 1981ApJ...250..615C.

[20] Mesa-Delgado, A., Esteban, C., García-Rojas, J., Reyes-Pérez, J., Morisset, C., and Bresolin, F., "THE TRACE OF THE CNO CYCLE IN THE RING NEBULA NGC 6888," *The Astrophysical Journal* **785**, 100 (Apr. 2014).

[21] Cristo, A., Plaza, A., and Valencia, D., "A novel thresholding method for automatically detecting stars in astronomical images," in [*2008 IEEE International Symposium on Signal Processing and Information Technology*], 180–185, IEEE (2008).

[22] Mould, J. R., "Infrared spectroscopy of M dwarfs.," **226**, 923–930 (Dec. 1978).

[23] Lancon, A. and Rocca-Volmerange, B., "A library of near-IR stellar spectra from 1.428 to 2.5 mu.m.," **96**, 593–612 (Dec. 1992).

[24] Meyer, M. R., Edwards, S., Hinkle, K. H., and Strom, S. E., "Near-Infrared Classification Spectroscopy: H-Band Spectra of Fundamental MK Standards," **508**, 397–409 (Nov. 1998).

[25] Developers, T., "Daostarfinder—photutils v0. 4," (2017).

[26] Gray, R., "A digital spectral classification atlas," (2000).

[27] Hamann, W.-R., Gräfener, G., and Liermann, A., "The Galactic WN stars-Spectral analyses with line-blanketed model atmospheres versus stellar evolution models with and without rotation," *Astronomy & Astrophysics* **457**(3), 1015–1031 (2006).

[28] Megier, A., Strobel, A., Bondar, A., Musaev, F., Han, I., Krełowski, J., and Galazutdinov, G., "Interstellar Ca II Line Intensities and the Distances of the OB stars," *The Astrophysical Journal* **634**(1), 451 (2005).